Linking rates of slab sinking to long-term lower mantle flow: Quantifying mantle mixing through configurational Entropy

Cedric Thieulot [1] Erik van der Wiel [1] Douwe J.J. van Hinsbergen [1]

[1]Department of Earth Sciences, Utrecht University, Princetonlaan 8A, 3584 CB Utrecht, the Netherlands

Utrecht University

Abstract

Numerical models of Earth's mantle dynamics that aim to comply with a variety of surface observations and/or modern mantle structure, still predict a **widely varying vigour of mantle flow** which governs the long-term evolution of mantle structure and mixing. A **yet unexplored source of information on mantle flow** characteristics are the geologically reconstructed average slab sinking rates.

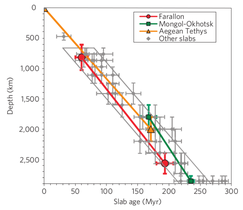

Figure 1. Age–depth curve of interpreted slabs. The symbols indicate slab limits, with error bars in age–depth interpretation. The grey box represents average sinking rate (∼ 12 mm/yr). van der Meer et al, Nature Geo. (2009)

We evaluate from numerical experiments how average slab sinking rates relate to the vigour of mantle convection and mixing. We use a simplified mantle convection model and show that **long-term mantle flow velocity and mixing is strongly sensitive to slab sinking rates**. Models tuned to match lower mantle average sinking rates of 10-15 mm/a yield lower mantle convection rates of only several mm/a. Furthermore, they reveal **large unmixed regions in the mid-mantle which preserve 25% of 'primordial' lower mantle material after 1000 Ma**, which may explain geochemical observations from hotspot volcanoes.

We explore the use of **configurational entropy**, based on tracer and compositional distribution on a global and local scale. We find that these entropy calculations may be used to quantitatively compare long-term geodynamic models with each other.

van der Wiel et al, EPSL, 2024

van der Wiel et al, Solid Earth, subm.

Methods

We performed numerical experiments in a **2D cylindrical geometry**, simulating **global mantle convection during 1000 Ma** of subduction evolution. These models are used to obtain slabs varying in size and shape and track their lower mantle sinking rates.

We solve the compressible flow equations of mass, momentum, and energy conservation:

$$\frac{\partial \rho}{\partial t} + \nabla \cdot (\rho u) = 0 \tag{1}$$

$$\nabla \cdot \sigma + \rho g = 0 \tag{2}$$

$$\rho C_p \left(\frac{\partial T}{\partial t} + u \cdot \nabla T \right) - \nabla \cdot (k \nabla T) = \rho H + S_s + S_a + S_l \tag{3}$$

with shear heating (S_s), adiabatic heating (S_a) and latent heating (S_l).

Computations were done using the finite element geodynamic code **ASPECT** (Kronbichler et al, 2012; Heister et al, 2017; Gassmöller et al, 2018).

Flow in our model is governed by the viscous-plastic flow equations that describe dislocation and diffusion creep and we use the Drucker-Prager yield criterion to limit viscous stresses (Glerum et al, 2018).

Both the inner and outer boundaries are free-slip boundaries.

The mantle domain consists of three different regions separated by the two major phase changes occurring at ~ 410 and ~ 660 km depths.

Particle-in-cell technique is used to track materials (Gassmöller et al, 2019).

CIG COMPUTATIONAL INFRASTRUCTURE for GEODYNAMICS `https://geodynamics.org/resources/aspect`

Results

We use three continents covering ∼30% of the model surface input with the geodynamic World Builder (Fraters et al, 2019). We run models with three viscosity profiles, P, R, and M:

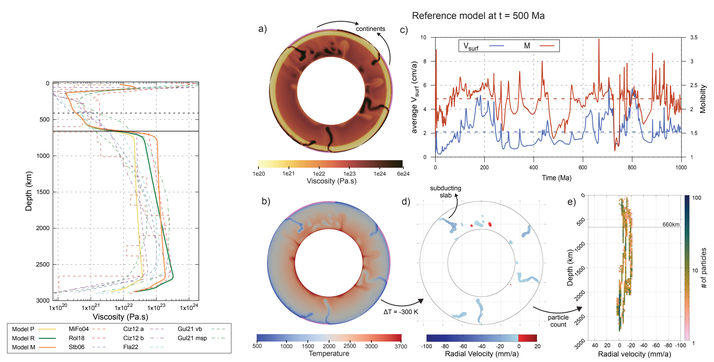

Figure 2. Left: Radial viscosity profiles for the three models discussed (solid lines: P - Poor, R - reference and M - Moderate) compared to viscosity profiles of other studies (see van der Wiel et al, 2024 for references). Right: Results of the reference model (R) after 500 Ma of simulation. Viscosity (**a**) and temperature (**b**) are shown within the modelled domain, showing five slabs actively subducting below the (pink) continents. (**c**) Solid lines indicate average surface velocity (blue) and mobility ratio M (Tackley, 2000) (red) of model R. (**d**) Radial velocity of all slab tracers plotted at their position in the model (blue: sinking slabs, red: slowly rising). Shown tracers are 300K colder than the radial averaged temperature at similar depth. (**e**) 2D-histogram showing the depth vs the radial velocity in 25 km by 2 mm/a bins of the tracers identified as slabs.

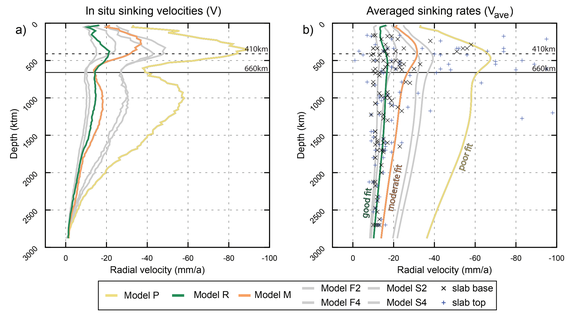

Figure 3. Profiles sinking velocities and averaged sinking rates matched with the data from van der Meer et al, 2028. (**a**) In situ sinking velocities calculated as depth average from the cumulative radial slab velocities. (**b**) Averaged slab sinking rates computed with $V_{ave}(d) = \frac{1}{d} \int_0^d V(z) dz$ compared to the slab data base (plus) and slab top (cross) data. The models with a good fit (model R – green), moderate fit (model M – orange) and poor fit (model P – yellow) are shown in colour together with all other S and F models in grey.

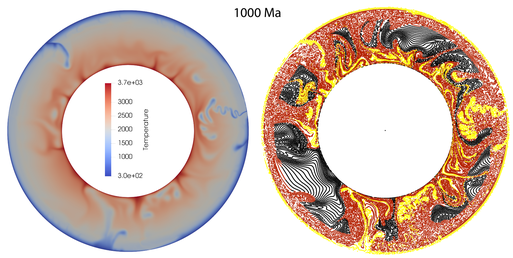

Figure 4. Snapshot from model R at $t = 1000$ Ma showing the temperature field in Kelvin (left) and passive particles colored by composition (lithosphere: yellow, upper mantle: red, lower mantle: black).

Configurational 'Shannon' entropy

We use configurational (or 'Shannon') entropy for quantifying compositional mixing of particles through flow on a global or local scale (Shannon, 1948; Camesasca et al, 2006; Naliboff & Kellogg, 2007).

The definition of the entropy S is based on the probability of a particle distribution in a domain tessellated by non-overlapping cells. The entropy depends on the distribution of particles, the number of cells M and the initial compositional distribution. Let C be the number of compositions. The entropy is calculated based on the discretized particle density $\rho_{c,j} = \frac{n_{c,j}}{N_c}$, i.e., the amount of particles of composition c in cell j, where N_c is the total number of c-particles divided by the number of cells M (this assumes that cells are of equal area, so N_c is the same for all cells). From the compositional density $\rho_{c,j}$ we calculate the conditional probability $P_{j,c}$ for finding a group of particles of composition c in cell j as well the probability for the cell-sum of compositional densities P_j

$$P_{j,c} = \frac{\rho_{c,j}}{\sum_{c=1}^{C} \rho_{c,j}} \qquad P_j = \frac{\sum_{c=1}^{C} \rho_{c,j}}{\sum_{j=1}^{M} \sum_{c=1}^{C} \rho_{c,j}}$$

We then define the global entropy S_{pd} of the particle distribution which quantifies the global spatial heterogeneity of the particle distribution independent of composition (Naliboff & Kellogg, 2007), and at the cell level, the local entropy S_j for cell j can be defined for the mixture of particles with different compositions:

$$S_{pd} = -\sum_{j=1}^{M} P_j \ln P_j \qquad S_j = -\sum_{c=1}^{C} P_{j,c} \ln P_{j,c}$$

Finally, the global entropy S of the particle distribution, accounting for composition, is the weighted average of P_j and the local entropy S_j: $S = \sum_{j=1}^{M} P_j S_j$.

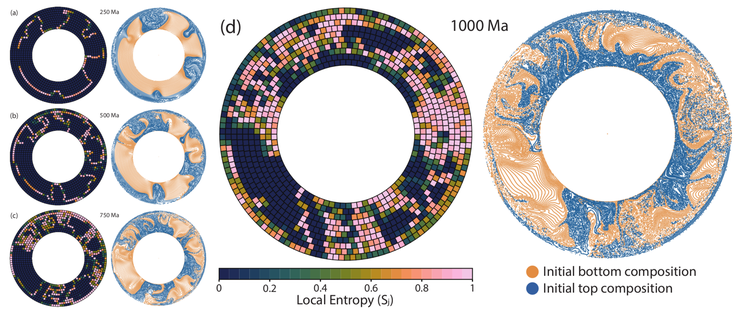

Figure 5. Local Entropy S_j (left) and particle distribution (right) at t=1000 Ma (model R) with a static 50/50 ratio particle composition at a resolution of 10x80 cells.

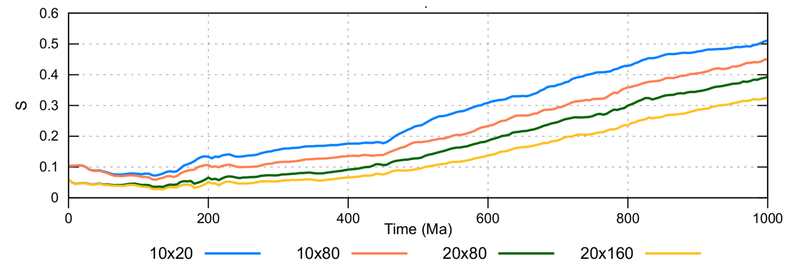

Figure 6. Global Entropy S of the model through time for different cell resolutions.